

YoloCurvSeg: You Only Label One Noisy Skeleton for Vessel-style Curvilinear Structure Segmentation

Li Lin, Linkai Peng, Huaqing He, Pujin Cheng, Jiwei Wu, Kenneth K. Y. Wong, Xiaoying Tang

Abstract—Weakly-supervised learning (WSL) has been proposed to alleviate the conflict between data annotation cost and model performance through employing sparsely-grained (i.e., point-, box-, scribble-wise) supervision and has shown promising performance, particularly in the image segmentation field. However, it is still a very challenging problem due to the limited supervision, especially when only a small number of labeled samples are available. Additionally, almost all existing WSL segmentation methods are designed for star-convex structures which are very different from curvilinear structures such as vessels and nerves. In this paper, we propose a novel sparsely annotated segmentation framework for curvilinear structures, named YoloCurvSeg, based on image synthesis. A background generator delivers image backgrounds that closely match real distributions through inpainting dilated skeletons. The extracted backgrounds are then combined with randomly emulated curves generated by a Space Colonization Algorithm-based foreground generator and through a multilayer patch-wise contrastive learning synthesizer. In this way, a synthetic dataset with both images and curve segmentation labels is obtained, at the cost of only one or a few noisy skeleton annotations. Finally, a segmenter is trained with the generated dataset and possibly an unlabeled dataset. The proposed YoloCurvSeg is evaluated on four publicly available datasets (OCTA500, CORN, DRIVE and CHASEDB1) and the results show that YoloCurvSeg outperforms state-of-the-art WSL segmentation methods by large margins. With only one noisy skeleton annotation (respectively 0.14%, 0.02%, 1.4%, and 0.65% of the full annotation), YoloCurvSeg achieves more than 97% of the fully-supervised performance on each dataset. Code and datasets will be released at <https://github.com/llmir/YoloCurvSeg>.

Index Terms—Sparse Annotation, One-shot, Curvilinear Structure Segmentation, Weakly-supervised Learning, Medical Image Synthesis.

I. INTRODUCTION

Curvilinear structures are elongated, curved, multi-scale structures that often appear tree-like and are commonly found in natural images (e.g., cracks and aerial road maps) and

This study was supported by the Shenzhen Basic Research Program (JCYJ20190809120205578); the National Natural Science Foundation of China (62071210); the Shenzhen Science and Technology Program (RCYX20210609103056042); the Shenzhen Basic Research Program (JCYJ20200925153847004); the Shenzhen Science and Technology Innovation Committee (KCXFZ2020122117340001).

Li Lin, Linkai Peng, Huaqing He, Pujin Cheng, Jiwei Wu and Xiaoying Tang are with the Department of Electronic and Electrical Engineering, Southern University of Science and Technology, Shenzhen, China and Jiaxing Research Institute, Southern University of Science and Technology, Jiaxing, China. Li Lin and Kenneth K. Y. Wong are also with the University of Hong Kong, Department of Electrical and Electronic Engineering, Hong Kong, China (linli@eee.hku.hk). Corresponding author: Xiaoying Tang (tangxy@sustech.edu.cn).

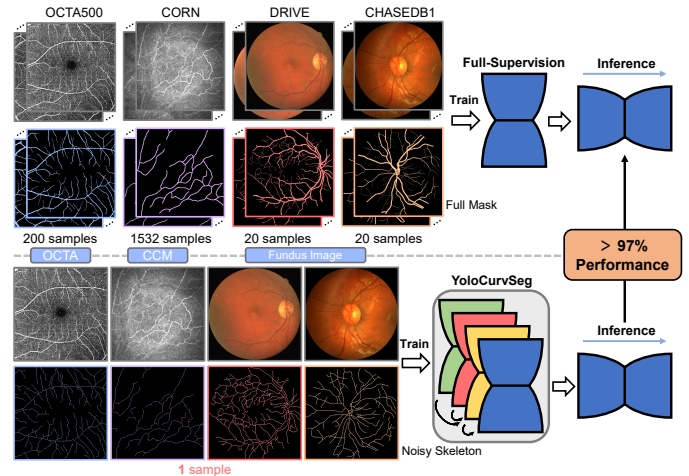


Fig. 1. YoloCurvSeg achieves more than 97% of the fully-supervised performance on each of four representative datasets utilizing only one noisy skeleton annotation, which means physicians can save more than 98% of the labeling time and still obtain satisfactory segmentation.

biomedical images (e.g., vessels, nerves and cell membranes). Automatic and precise segmentation of these curvilinear structures plays a significant role in both computer vision and biomedical image analysis. For example, road mapping serves as a prerequisite in both autonomous driving and urban planning. In the biomedical field, studies [1]–[4] have suggested that the morphology and topology of specific curvilinear anatomy (e.g., retinal vessels and corneal nerve fibers) are highly relevant to the presence or severity of various diseases such as hypertension, arteriosclerosis, keratitis, age-related macular degeneration, diabetic retinopathy, and so on. Retinal vessels are observable in retinal fundus images and optical coherence tomography angiography (OCTA) images, while corneal nerve fibers are identifiable in confocal corneal microscopy (CCM) images. It has been suggested that early signs of many ophthalmic diseases are reflected by microvascular and capillary abnormalities [5], [6]. Collectively, accurate segmentation of various curvilinear structures is of great importance for computer-aided diagnosis, quantitative analysis and early screening, especially in ophthalmology.

In recent years, benefiting from the development of deep learning (DL), many DL-based segmentation algorithms for curvilinear structures have been proposed and have shown overwhelming performance compared to traditional (e.g., matched filter-based and morphological processing-based [7], [8]) methods. Most existing works are dedicated to designing sophisticated network architectures [9]–[11] or deploying strategies to preserve curvilinear structures' topology by employing generative adversarial networks (GANs) [2],

[12] or topology-preserving loss functions [13], [14]. These methods are typically fully-supervised, wherein large-scale well-annotated datasets are required. However, collecting and labeling a large-scale dataset with full annotation is very costly and time-consuming, particularly for medical images since their annotation requires expert knowledge and clinical experience. Furthermore, annotating curvilinear structures is even more challenging, given that curvilinear structures are slender, multi-scale, and complex in shape with fine details.

More recently, many efforts have been made to reduce the annotation cost for DL model training. For example, semi-supervised learning (SSL) trains models by combining limited amounts of annotated data with massive unlabeled data [15]–[17]. While effective, most state-of-the-art (SOTA) SSL methods still require about 5%-30% of the accurately and precisely labeled data to achieve about 85%-95% of the fully-supervised performance, which is still not sufficiently cost-effective and still time-consuming when it comes to labeling curvilinear structures. Weakly supervised learning (WSL) attempts to alleviate the annotation issue from another perspective by performing sparsely-grained (i.e., point-, scribble-, bounding box-wise) supervision and attains promising performance [18]–[22]. Compared with either point or bounding box, scribble is a relatively more flexible and generalizable form of sparse annotation that can be used to annotate complex structures [23]. Existing scribble-supervised segmentation methods mainly fall into two categories. The first line of research exploits structural or volumetric priors to expand scribbles into more accurate pseudo proposals; for example, grouping pixels with similar grayscale intensities or locations into the same class [18], [19], [24]. However, the expansion process may introduce noisy proposals, which may induce error accumulation and deteriorate the performance of the segmentation model. Some work [25] also points out the inherent weakness of these methods, namely models retain their own predictions and thus resist updating. The second line learns adversarial shape priors utilizing extra unpaired but fully-annotated masks. Such approaches somewhat contradict the motivation of saving annotation costs, especially for complex curvilinear structures [26]–[28]. Moreover, most WSL methods still require sparsely labeling the entire dataset (or a large portion), and they are mainly designed and validated on relatively simple structures (e.g., cardiac structures or abdominal organs) with assumptions and priors that may not apply to complex structures (e.g., curvilinear structures).

To address these aforementioned challenges, we here present a novel WSL segmentation framework for vessel-style curvilinear structures, namely *You Only Label One Noisy Skeleton for Curvilinear Structure Segmentation* (*YoloCurvSeg*). For curvilinear structures, label noises/errors are inevitable, and a good segmentation approach should be noise tolerant. Therefore, instead of utilizing only the annotated pixels for supervision, YoloCurvSeg ingeniously converts the weakly-supervised problem into a fully- or semi-supervised one via image synthesis. It employs a trained inpainting network as a background generator, which takes one (or multiple depending on availability) noisy skeleton (as shown in Fig. 1) and dilates it to serve as an inpainting mask to

obtain a background that closely matches the real distribution. The extracted background is then augmented and combined with randomly emulated curves generated by a Space Colonization Algorithm-based foreground generator, from which a synthetic dataset is obtained through a multilayer patch-wise contrastive learning synthesizer. Finally, a segmenter performs coarse-to-fine two-stage training using the synthetic dataset and an unlabeled dataset (if available). Our main contributions are summarized as follows:

- We propose a novel weakly-supervised framework for one-shot skeleton/scribble-supervised curvilinear structure segmentation, namely YoloCurvSeg. To the best of our knowledge, YoloCurvSeg is the first sparsely-annotated and weakly-supervised segmentation method for curvilinear structures.
- YoloCurvSeg novelly converts a WSL problem into a fully supervised one through four steps: curve generation, image inpainting, image translation and coarse-to-fine segmentation. The proposed framework is noise-robust, sample-insensitive and easily extensible to various curvilinear structures.
- We evaluate YoloCurvSeg on four challenging curvilinear structure segmentation datasets, namely OCTA500 [29], CORN [30], DRIVE [31], CHASEDB1 [32]. Experimental results show that YoloCurvSeg outperforms SOTA WSL and noisy label learning methods by large margins. Meanwhile, we demonstrate that $> 97\%$ of the fully-supervised performance can be achieved with only one noisy skeleton label (approximately 0.1% or 1% of the full annotation).

II. RELATED WORKS

A. Curvilinear Structure Segmentation

Existing automatic curvilinear structure segmentation algorithms can be roughly divided into two categories. The first category is traditional unsupervised methods, mainly including mathematical morphology methods and various filtering methods [10]. For instance, Zana et al. [33] segment vascular-like patterns using a hybrid framework of morphological filtering and cross-curvature analysis. Passat et al. [34] present a preliminary approach to strengthen the segmentation of cerebral vessels by incorporating high-level anatomical knowledge into the segmentation process. Filtering methods include Hessian matrix-based filters [35], matched filters [8], [36], multi-oriented filters [37], symmetry filter [38], etc. The other category is supervised methods, wherein data with ground truth labels are used to train segmenters based on predefined or model-extracted features. Traditional machine-learning-based approaches are dedicated to pixel-level classification using handcrafted features [39], [40]. Recently, DL-based approaches have made significant progress in various segmentation tasks. For example, Ronneberger et al. [41] propose U-Net, which has been widely used in numerous medical image segmentation tasks. Existing curvilinear structure segmentation works focus on well-designed network architectures by introducing multi-scale [11], [42], multi-task [6], [9], [43], or various attention mechanisms [10], [44]

and well-playing morphological and topological properties by introducing GANs or morphology-/topology-preserving loss functions [13], [14]. Still, data availability and annotation quality are the main limitations of these methods.

B. Weakly-supervised Segmentation

Weakly-supervised segmentation aims to reduce the labeling costs by training segmentation models on data annotated with coarse granularity [18]. Among various formats of sparse annotations, scribble is recognized as the most flexible and versatile one that can be used to annotate complex structures [23], [27]. Existing scribble-supervised segmentation methods fall into two main categories. The first one exploits structural or volumetric priors to expand scribble annotations by assigning a same class to pixels with similar intensities or nearby locations [18], [19], [24]. The main limitation of such approaches is that they heavily rely on pseudo proposals and often contain multiple stages, which can be time-consuming and prone to errors that may be propagated during model training. The second category learns adversarial shape priors utilizing extra unpaired but fully-annotated masks. Such approaches somewhat contradict the motivation of saving annotation costs, especially for complex curvilinear structures [26]–[28]. Additionally, these methods still require sparsely labeling the entire dataset or a large portion, and they are mainly designed and validated on relatively simple structures like cardiac structures or abdominal organs with assumptions and priors that may not apply to complex structures (e.g., curvilinear structures). In this paper, we make use of noisy skeletons that differ from scribbles in two ways: (1) skeletons are more label demanding since all branches are supposed to be covered; (2) they are more likely to contain errors or noises, which are inevitable when quickly labeling slender structures. We convert sparse and noisy skeleton annotations to accurate ones via an image synthesis pipeline, thus requiring only one noisy skeleton label. This significantly reduces the annotation cost.

C. Medical Image Synthesis

GAN [45] has become the mainstay of medical image synthesis, with common applications in intra-modality augmentation [46], cross-domain image-to-image translation [47], quality enhancement [48], missing modality generation [49], etc. Below we briefly review previous works on retinal image synthesis, the topic of which is relevant to our work. Costa et al. [50] employ a U-Net trained with paired fundus images and vessel masks. It employs a conditional GAN (Pix2pix [52]) to learn a mapping from vessel masks to the corresponding fundus images. To simplify the framework, they propose an adversarial autoencoder (AAE) for retinal vascularity synthesis and a GAN for generating retinal images [51]. Similarly, Guibas et al. [53] present a two-stage approach that consists of a DCGAN for generating vasculature from noise and a cGAN (Pix2pix) to synthesize the corresponding fundus image. These methods require an extra set of vessel annotations to train AAE or DCGAN and may sometimes generate vessels with unrealistic morphology. The generated images also lack diversity. Zhao

et al. [54] develop Tub-sGAN, which incorporates style transfer into the GAN framework to generate more diverse outputs. Note that cGAN requires paired images and vessel masks for training, which is a strict condition to some extent. In another work, SkrGAN [55] is proposed to introduce a sketch prior related constraint to guide the image generation process. Yet, the sketches utilized are extracted by the Sobel edge operator, and cannot be used as segmentation masks. In this paper, we employ a multilayer patch-wise contrastive foreground-background fusion GAN for several considerations. According to previous research, training a GAN to learn a direct mapping from a curvilinear structure mask to the corresponding image is difficult, especially under few-shot conditions [56]. Therefore, we provide GAN with extracted real backgrounds, enabling implicit skip-connection that allows the GAN to focus more on mapping the foreground regions. Such a design not only enhances performance but also accelerates convergence. Multilayer patch-wise contrastive learning allows the provided mask and the foreground region of the generated image to be spatially aligned (via unpaired training), which further benefits the subsequent segmenter.

III. PROPOSED METHOD

YoloCurvSeg comprises four main components: (1) a *Curve Generator* that produces binary curve masks that well accommodate the corresponding image modality of interest; (2) an *Inpainter* for extracting backgrounds from labeled samples; (3) a *Synthesizer* that synthesizes images from the generated curve masks and the image backgrounds; and (4) a two-stage *Segmenter* trained with the synthetic dataset and an unlabeled dataset. The overall framework is shown in Fig. 2.

A. Curvilinear Structure Generation

Space colonization is a procedural modeling algorithm in computer graphics that simulates the growth of branching networks or tree-like structures [57], [58], including vasculature, leaf venations, root systems, etc. It is employed in YoloCurvSeg for modeling the iterative growth of curvilinear structures with two fundamental elements: attractors and nodes. Its core steps are described in the top left panel of Fig. 2, wherein blue dots denote attractors and black ones denote nodes: a) place a set of attractors randomly or following a predefined pattern, and then associate nodes with nearby attractors (if their distance is within an attraction distance D_a); b) for each node, calculate its average direction from all attractors affecting it; c) calculate the position of new nodes via normalizing the average direction to a unit vector and scaling it by a pre-defined *segment length* L_s ; d) place nodes at the calculated positions and check if any nodes are within an attractor's kill zone; e) prune an attractor if there are nodes staying within its *kill distance* D_k ; f) repeat steps b)-e) until the maximum number of nodes is reached. Given predefined bounds and obstacles, we can simulate various curvilinear structures by adjusting the parameters D_a , D_k , L_s and the root node coordinates C_r . Table I summarizes the parameters and post-processing operations we employ for generating the four types of curves and representative examples are demonstrated

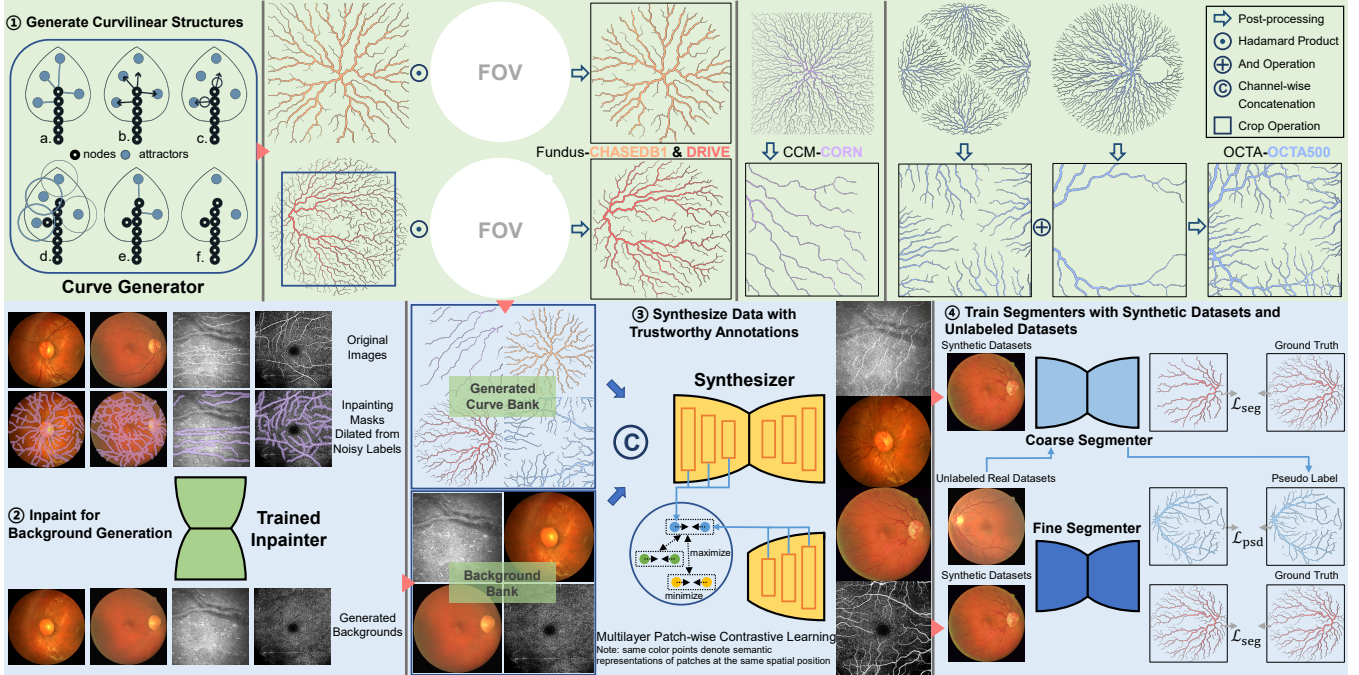


Fig. 2. Overview of our proposed YoloCurvSeg, which comprises four main components: a space colonization algorithm-based curve generator, a background inpainter, a multilayer patch-wise contrastive foreground-background fusion synthesizer, and a two-stage coarse-to-fine segmenter.

in the top panel of Fig. 2. In addition to the curvilinear shape, we also need to simulate the thickness of each branch

$$R^n = R_1^n + R_2^n, \quad (1)$$

where R , R_1 and R_2 respectively denote the radii of a father branch and its two child branches. n is set to be 3 according to Murray's law [59]. The calculation is performed recursively from the branch tips (whose radii are set to be 1) towards the tree base. Several intuitive demos can be accessed at link¹. By setting random grid attractors and root nodes via predefined parameters, we construct four curve banks for our four datasets of interest, which are then utilized for training the *synthesizers* and the *segmenters*.

B. Inpainting for Background Extraction

Inpainting is the task of reconstructing missing or masked regions in an image. Similar to removing watermarks or extraneous pedestrians from images, we employ an inpainting model here to remove foregrounds (e.g., vessels and nerve fibers) from the images of interest, under the hypothesis that the dilated noisy skeletons can fully cover the foregrounds. In inpainting, common concerns are the network's ability to grasp local and global context and to generalize to a different (especially higher) resolution.

1) *Architecture*: Inspired by [60], we adopt an inpainting network based on the recently proposed *fast Fourier convolutions* (FFCs) [61] with image-wide receptive fields, strong generalizability and relatively few parameters. Given a masked image $I \odot (1 - m)$, where I and m respectively denote the original image and the binary mask of inpainting regions, the feed-forward inpainting network $f_\theta(\cdot)$ aims to output an inpainted image $\hat{I} = f_\theta(I')$ taking a four-channel input $I' = \text{concat}(I \odot (1 - m), m)$. FFC builds its basis on channel-wise fast Fourier transform (FFT) and has a receptive field covering the whole image. It splits channels into two parallel branches: a *local* branch uses conventional convolutions and

a *global* branch uses *real* FFT to capture global context, as shown in Fig. 3. *real* FFT is only applicable to real-valued signals, and inverse *real* FFT ensures the output is real-valued. Compared to FFT, *real* FFT uses only half of the spectrum. In FFC, *real* FFT is first applied to the input tensor and a *ComplexToReal* operation is performed by concatenating the real and imaginary parts. Then, it applies convolutions in the frequency domain. Inverse *real* FFT is performed to transform features from the frequency domain to the spatial domain through the *RealToComplex* operation. Finally, the local and global branches are fused. For the upsampling and downsampling of the *Inpainter* and the discriminator architecture in adversarial training, we follow the ResNet settings respectively employed in [62] and [60]. The training is performed on [image, randomly synthesized mask] pairs. We adopt the mask generation strategy in [60], containing multiple rectangles with arbitrary aspect ratios and wide polygonal chains.

2) *Objective*: Compared with naive supervised losses which may result in blurry predictions, perceptual loss [63] evaluates the distance between feature maps of the inpainted image and the original image via a pre-trained network $\phi(\cdot)$. It does not require exact reconstruction and allows for variations in the reconstructed image. Given that inpainting focuses on understanding the global structure, we introduce a perceptual loss of a large receptive field \mathcal{L}_{HRP} through a pre-trained ResNet50 $\phi_{HRF}(\cdot)$ with dilated convolutions provided in [60]

$$\mathcal{L}_{HRP}(I, \hat{I}) = \mathcal{M}([\phi_{HRF}(I) - \phi_{HRF}(\hat{I})]^2), \quad (2)$$

where \mathcal{M} is a sequential two-stage mean operation, i.e., obtaining the inter-layer mean of intra-layer means. Additionally, an adversarial loss \mathcal{L}_{adv} is utilized to encourage the inpainted image to be realistic. Specifically, we use a PatchGAN [52] discriminator $\mathcal{D}_\xi(\cdot)$ and label patches that overlap with the mask as *fake* and the others as *real*. The non-saturating adversarial loss is defined as

$$\mathcal{L}_D = -E_I[\log D_\xi(I)] - E_{I,m}[\log D_\xi(\hat{I} \odot (1 - m))] - E_{I,m}[\log(1 - D_\xi(\hat{I})) \odot m], \quad (3)$$

¹<https://jasonwebb.github.io/2d-space-colonization-experiments/>

TABLE I

PARAMETERS FOR GENERATING DIFFERENT TYPES OF CURVES. D_a , D_k , L_s and C_r RESPECTIVELY DENOTE THE ATTRACTION DISTANCE, KILL DISTANCE, SEGMENT LENGTH AND ROOT NODE COORDINATES. r AND l DENOTE RADIUS AND LENGTH. \oplus AND \odot REPRESENT THE UNION AND ELEMENT-WISE MULTIPLICATION OPERATIONS. THERE ARE TWO ROWS FOR OCTA500 SINCE TWO COMPONENTS ARE NEEDED.

Dataset	Bound	Obstacle	C_r	D_a	D_k	L_s	Post-processing
OCTA500	Circle, $r = 450$	-	Midpoints of the Four Sides	5	30	5	Crop, \oplus
	Circle, $r = 450$	Circle with Center (650,450), $r \in [60, 90]$	$x, y \in [\frac{1}{2}r - 150, \frac{1}{2}r + 150]$				
CORN	Square, $l = 1300$	-	$x, y \in [\frac{1}{2}l - 30, \frac{1}{2}l + 30]$	5	30	5	Random Crop
DRIVE	Circle, $r = 400$	Concentric Circle, $r \in [40, 60]$	$x \in [\frac{1}{4}r - 30, \frac{1}{4}r + 30], y \in [r - 50, r + 50]$	5	30	5	\odot FOV, Random Flip
CHASEDB1	Square, $l = 960$	-	$x, y \in [\frac{1}{2}l - 40, \frac{1}{2}l + 40]$	3	35	10	\odot FOV, Dilate

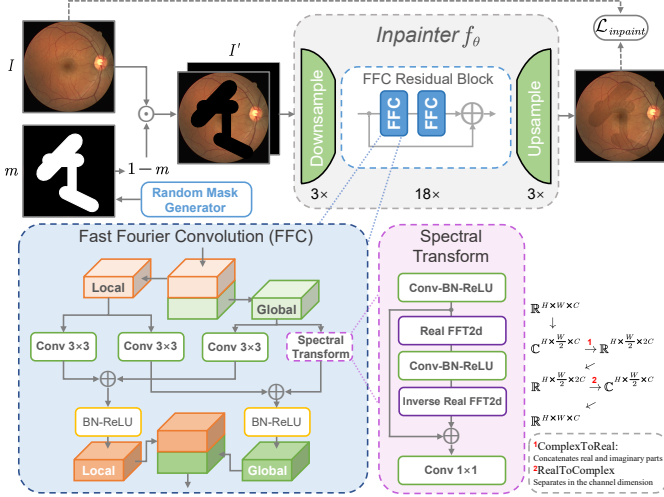


Fig. 3. The architecture of the *Inpainter*. The input is a four-channel image with the first three channels being the original image and the last channel being the binary mask of the inpainting regions. The output is the inpainted image. The dimensional change of the feature map in FFC is shown in the lower right panel.

$$\mathcal{L}_G = -E_{I,m}[\log D_\xi(\hat{I})], \quad (4)$$

$$\mathcal{L}_{adv} = \text{sg}_\theta(\mathcal{L}_D) + \text{sg}_\xi(\mathcal{L}_G) \rightarrow \min_{\theta, \xi}, \quad (5)$$

where $\hat{I} = f_\theta(I')$ is the output of the inpainting network and sg_{var} represents stop gradient w.r.t. var . To further stabilize the training, we use a gradient penalty $\mathcal{L}_{GP} = E_I \|\nabla D_\xi(I)\|_2^2$ [64] and a perceptual loss defined on features of the discriminator \mathcal{L}_{DP} [65]. The final objective of the *Inpainter* is

$$\mathcal{L}_{inpaint} = \mathcal{L}_{HRP} + \lambda_{adv}\mathcal{L}_{adv} + \lambda_{DP}\mathcal{L}_{DP} + \lambda_{GP}\mathcal{L}_{GP}, \quad (6)$$

where λ_{adv} , λ_{DP} and λ_{GP} are hyper-parameters balancing the contributions of different losses. \mathcal{L}_{HRP} is responsible for supervised signals and global structure consistency while \mathcal{L}_{adv} and \mathcal{L}_{DP} are responsible for local details and realism.

3) Training: Given that the training of the *Inpainter* does not require annotation and it learns a general ability to recover missing regions through contextual understanding, we employ a unified *Inpainter* pre-trained on the Places-Challenge dataset [66] and fine-tune on the combination of our four datasets of interest. The training is conducted with a batch size of 8 and an Adam optimizer is adopted with a learning rate of 10^{-3} for 50 epochs. The training data are augmented through random flipping, rotation and color jittering. We empirically set $\lambda_{adv} = 3$, $\lambda_{DP} = 10$ and $\lambda_{GP} = 10^{-4}$. Once trained, the *Inpainter* is used to remove the foregrounds from the skeleton-labeled samples taking the dilated noisy annotations as the masks. Then we construct a background bank for each dataset by augmenting the extracted backgrounds through random flipping, rotation, etc.

C. Patch-wise Contrastive Learning Based Synthesis

Now we have a curve (foreground) bank $B_{curv} = \{c^1, \dots, c^N\}$ and a background bank $B_{bg} = \{b^1, \dots, b^N\}$ respectively from the *Curve Generator* and the *Inpainter*, for each given dataset. We construct an intermediate dataset $X_{inter} = \{x^1, \dots, x^N\}$ through randomly sampling a curve c^i from B_{curv} and a background b^i from B_{bg} , and then concatenating them to form a temporary sample $x^i = \text{concat}(b^i, c^i)$. The problem now turns into an unpaired image-to-image translation task, i.e., designing a synthesizer to learn a mapping from X_{inter} to the corresponding real dataset Y . It is desirable that the local context especially the foreground of the synthetic image \hat{y}^i is spatially aligned with that of the corresponding intermediate image x^i (especially c^i) as much as possible.

Previously, for unpaired image translation, most existing methods apply GANs with a cycle structure, relying on cycle-consistency to ensure high-level correspondence [67]. While effective, the underlying bijective assumption behind cycle-consistency is sometimes too restrictive, which may reduce the diversity of the generated samples. More importantly, the cycle-consistency is not suitable for our task since it does not guarantee any explicit or implicit spatial constraints. In such context, we introduce a multilayer patch-wise contrastive learning based synthesizer to learn a mapping from X_{inter} to Y inspired by [68], [69], which is illustrated in the lower middle panel of Fig. 2. It is trained in a generative adversarial manner with an internal contrastive learning pretext task.

The generator (i.e., synthesizer) G is a U-shape network, which firstly down-samples the input image into high-level features via an encoder E with three residual blocks equipped with instance normalization and ReLU activation. As such, each pixel in the high-level feature map represents the embedding feature vector of a patch in the original image. Several layers of interest $E_{l \in L}(x)$ in E are selected to extract multi-scale features of patches and each passes through a two-layer multilayer perceptron (MLP) H_l (l indexes a layer), obtaining a feature stack $\{v_{l \in L} = H_{l \in L}[E_{l \in L}(x)]\}$. Given patchwise features v_l and the corresponding pair $\{H_l(E_l(x))^{s_1}, H_l(E_l(G(x)))^{s_2}\}$ with s_1 and s_2 denoting the spatial locations of the patches of interest, we set v^+ to represent a patch at the same location as v and v_n^- to denote the n^{th} among N patches at different locations. The objective of the contrastive learning task is to maintain the local information at the same spatial location. Similar to the noise contrastive estimation loss [70], our objective function can be written as

$$\mathcal{L}_c = - \sum_{l \in L} \log \frac{\exp(v_l \cdot v_l^+ / \tau)}{\exp(v_l \cdot v_l^+ / \tau) + \sum_{n=1}^N \exp(v_l \cdot v_n^- / \tau)}, \quad (7)$$

where τ is a temperature hyper-parameter. Besides, we employ the identity loss, which was first proposed in [67] for regularizing the generator G . We pass each real sample $y \in Y$ through the encoder E and obtain the patchwise features v^* , the negative samples v^{*-} and the positive samples v_n^{*+} . The identity loss is formulated as

$$\mathcal{L}_{id} = -\sum_{l \in L} \log \frac{\exp(v_l^* \cdot v_l^{*+} / \tau)}{\exp(v_l^* \cdot v_l^{*+} / \tau) + \sum_{n=1}^N \exp(v_l^* \cdot v_{ln}^{*-} / \tau)}. \quad (8)$$

We use the LSGAN loss as our adversarial loss \mathcal{L}_{adv} [71] to make the synthetic images as realistic as possible. Therefore, with trade-off parameters λ_{adv} , λ_c and λ_{id} , the overall loss of the synthesizer is defined as

$$\mathcal{L}_{syn} = \lambda_{adv} \mathcal{L}_{adv} + \lambda_c \mathcal{L}_c + \lambda_{id} \mathcal{L}_{id}. \quad (9)$$

The training of the synthesizer is conducted employing an Adam optimizer with a learning rate of 10^{-4} and a cosine decay strategy, together with a batch size of 1. We set λ_{adv} as 1, λ_c as 1, λ_{id} as 0.5 and τ as 0.07. The training process is stopped after 300 epochs.

D. Two-stage Coarse-to-Fine Segmentation

A synthetic dataset $\mathcal{D}_{syn} = \{(\hat{y}^1, c^1), \dots, (\hat{y}^N, c^N)\}$, with \hat{y}^i being a synthetic image and c^i being the corresponding curve ground truth, is created by the *Synthesizer*. The weakly-supervised task is then transformed into a fully- or semi-one when making use of solely the synthetic dataset or a combination of an unlabeled dataset \mathcal{D}_{ori} and the synthetic dataset \mathcal{D}_{syn} . In this section, we introduce a two-stage coarse-to-fine segmentation pipeline to tackle the task.

A specific segmentation network is first trained on \mathcal{D}_{syn} to obtain a coarse model S_{coarse} with a segmentation loss \mathcal{L}_{seg}

$$\mathcal{L}_{seg} = 0.5 \times \mathcal{L}_{ce} + 0.5 \times \mathcal{L}_{dice}, \quad (10)$$

where \mathcal{L}_{ce} and \mathcal{L}_{dice} respectively denote the cross-entropy loss and the Dice loss. We observe and conclude that the performance of S_{coarse} is mainly limited by two issues; one is that the curve generated by the *Curve Generator* still has a certain **morphological gap** with the foreground of the real image, and the other one is that there is also a slight but inevitable **intensity gap** between the *Synthesizer*-generated image and the real image. We target at relieving the latter issue by making use of \mathcal{D}_{ori} to further boost the segmentation performance. We employ predictions on \mathcal{D}_{ori} from S_{coarse} as pseudo-labels and train a fine model S_{fine} (initialized on S_{coarse}) on the combination of \mathcal{D}_{ori} and \mathcal{D}_{syn} via a final loss \mathcal{L}_{final} which is formulated as

$$\mathcal{L}_{final} = \mathcal{L}_{seg} + \lambda_{psd} \mathcal{L}_{psd}, \quad (11)$$

where \mathcal{L}_{psd} denotes the loss on \mathcal{D}_{ori} sharing the same formulation as \mathcal{L}_{seg} in Eq. (10) and λ_{psd} is a trade-off parameter. We employ vanilla U-Net with feature channels of 16, 32, 64, 128 and 256 as our S_{coarse} 's and S_{fine} 's architecture. We use an SGD optimizer (weight decay = 10^{-4} , momentum = 0.9) for training both S_{coarse} and S_{fine} with a batch size of 12 and an initial learning rate of 10^{-2} . The total iterations and λ_{psd} are respectively set to be $30k$ and 1.

IV. EXPERIMENTS

In this section, we extensively evaluate the effectiveness of our YoloCurvSeg framework on four representative curvilinear structure segmentation datasets.

A. Datasets and Preprocessing

We comprehensively evaluate YoloCurvSeg on four ophthalmic datasets: OCTA500, CORN, DRIVE and CHASEDB1. OCTA500 is used for retinal microvascular segmentation, and only the subset that contains 300 samples with a $6 \times 6 \text{ mm}^2$ field of view (FOV) and a 400×400 resolution is utilized. We only make use of the OCTA *en-face* images generated by maximum projection between the internal limiting membrane layer and the outer plexiform layer. CORN consists of 1578 CCM images for nerve fiber segmentation. It also provides two subsets respectively consisting of 340 low-quality and 288 high-quality images. All CCM images have a resolution of 384×384 and an FOV of $400 \times 400 \mu\text{m}^2$. Instead of following the dataset's original division, we use 1532 images (samples that overlap with the test set are removed and the validation split ratio is 0.2) for training and validation, and test on 60 relatively accurately labeled samples provided in its subset. DRIVE and CHASEDB1 are used for retinal vessel segmentation and respectively have resolutions of 565×584 and 999×960 . These two fundus datasets are cropped via the provided FOV masks and respectively resized to 576×576 and 960×960 . We normalize the intensity of each image to 0-1. Data augmentation consists of random rotation, flipping and Bézier Curve transformation [72].

B. Implementation Details

We implement YoloCurvSeg and other compared methods by PyTorch on a workstation equipped with 8 RTX 3090Ti GPUs. In the *Synthesizer*, the indices of the layers selected to calculate \mathcal{L}_c include $\{0, 4, 8, 12, 16\}$. For training the *Segmenters* S_{coarse} and S_{fine} , the polynomial policy with $power = 0.9$ is used to adjust the learning rate online [73]. Other hyperparameters, training details and model architecture are already provided in previous sections. It is worth noting that manually-delineated vessel segmentation labels are provided for OCTA500, DRIVE and CHASEDB1. To generate noisy skeleton annotations for those three datasets, we perform the *skeletonize* operation in *scikit-image* [74] to obtain the skeletons of the original ground truth masks and then employ *elastic transformation* to simulate jitter noises that may be introduced during fast manual labeling. For CORN, only noisy skeleton labels are provided, and thus are directly used in all our experiments. For this dataset, we dilate each skeleton to a 3-pixel width to serve as the full mask in its fully-supervised learning setting, and the same operation is also applied to the testing set annotations. For sparse labels used in other comparative WSL methods, skeletons of the backgrounds are also generated via skeletonization. The synthesis process in YoloCurvSeg can be online or offline. For better reproducibility and fair comparison, we use the offline version in our experiments, i.e., we first generate the synthetic dataset and then train the *Segmenters*. We generate 1276, 5005, 1240, and

1604 synthetic samples respectively for OCTA500, CORN, DRIVE and CHASEDB1 if all training samples are labeled. If only one sample is labeled, we respectively generate 100, 100, 60, and 80 synthetic samples.

C. Synthesis Performance

Before comparing with SOTA WSL methods, we first qualitatively and quantitatively evaluate the synthesis performance of YoloCurvSeg. We visualize representative examples, in terms of the noisy skeleton labels, dilated masks for inpainting, extracted backgrounds, generated curves and synthesized images, in Fig. 4. It can be observed from the last column that the generated curves well match the synthetic images. We also compare the intensity distributions of the synthetic datasets with the real ones in Fig. 5, exhibiting high intensity similarities between the synthetic and real images in terms of both background and foreground. From the t-SNE [75] visualization in Fig. 6, the synthetic datasets are generally in line and well mixed with the real ones. In most cases, the synthetic data are even more uniformly and widely distributed, having a similar effect as data augmentation. The Fréchet Inception Distances (FIDs) [76] between the synthetic components and the corresponding real ones are tabulated in Table II to measure the difficulty of learning a mapping between the two distributions. Column A shows the morphological gap between the synthetic and real curvilinear structures. Columns B and C illustrate there is great difficulty in translating directly to the image distribution from foreground masks, while the background image with the foreground removed is less distant from the original distribution. Since YoloCurvSeg incorporates background information, which implicitly acts as skip connections, it reduces the difficulty of image translation and thus can synthesize images close to the real ones even under few-shot settings. Our method achieves competitive FID scores on all four datasets, two of which are even smaller than those between the real training and test sets, as shown in column E of Table II.

D. Comparisons with SOTA

Since noisy skeletons can be considered as sparse annotations with a certain degree of noise or directly utilized as

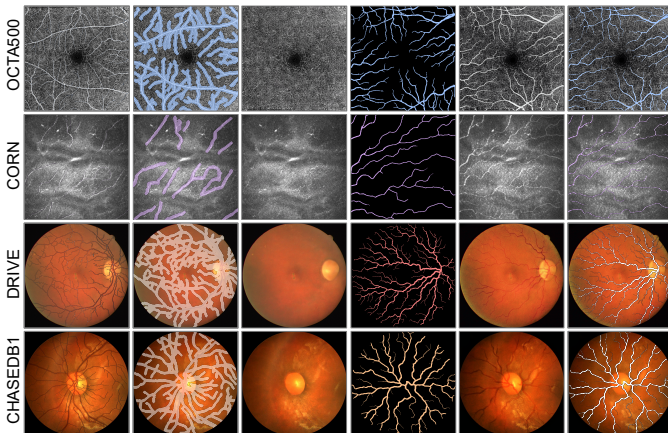


Fig. 4. Visualization of synthetic data from YoloCurvSeg. From left to right are examples of the noisy skeleton label, the inflated inpainting mask, the extracted background, the generated foreground, the synthesized image and the generated foreground superimposed on the synthesized image. Zoom in for details.

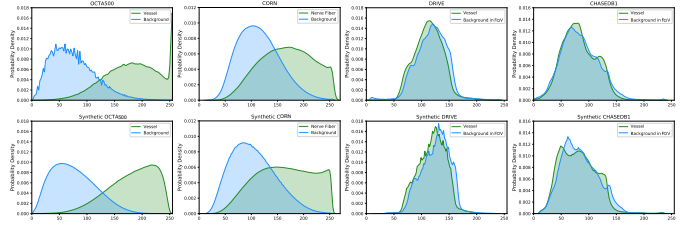


Fig. 5. Histograms of the four datasets in terms of the real data (top) and the corresponding synthetic data (bottom).

TABLE II

FID SCORES BETWEEN VARIOUS SYNTHETIC COMPONENTS AND THE REAL ONES. A: SYNTHETIC MASK VS. REAL MASK, B: SYNTHETIC MASK VS. REAL IMAGE, C: SYNTHETIC BACKGROUND VS. REAL IMAGE, D: SYNTHETIC IMAGE VS. REAL IMAGE, E: REAL TRAINING IMAGE VS. REAL TEST IMAGE.

Dataset	A	B	C	D	E
OCTA500	44.93	202.82	195.66	40.88	25.89
CORN	97.17	313.04	174.42	38.26	60.91
DRIVE	157.53	298.93	143.69	67.91	51.49
CHASEDB1	165.74	367.72	136.29	56.11	75.96

noisy labels, we compare YoloCurvSeg with two categories of methods: 1) WSL methods and 2) noisy label learning (NLL) methods. The Dice similarity coefficient (DSC) and the average symmetric surface distance (ASSD) are used as the evaluation metrics.

1) *Comparison with WSL methods*: Firstly, we compare YoloCurvSeg with 11 scribble-supervised segmentation methods employing the same skeleton set that we generate: pCE (baseline); random walker pseudo labeling (RW); uncertainty aware self-ensembling and transformation-consistent model (USTM); Scribble2Label (S2L); Mumford–shah Loss (MLoss); entropy minimization (EM); dense CRF loss and gated CRF loss; active contour loss (AC); dual-branch network with dynamically mixed pseudo labels supervision (DBDM) and tree energy loss, the results of which are shown in Table III. For fair comparisons, YoloCurvSeg does not go through the fine stage and is denoted as *Ours (coarse)* (i.e., the performance of S_{coarse}). The upper part of the table indicates that all training data are sparsely labeled, while the lower part indicates that only one representative sample is labeled and all other data are unlabeled and not utilized. YoloCurvSeg achieves the best performance on all datasets under both settings, outperforming other WSL methods by **large margins**. Comparing "All" versus "One", apparently, YoloCurvSeg is not sensitive to the sample size of the labeled data and achieves **96.2%**, **106.3%**, **95.3%** and **96.2%** fully-supervised performance on the four datasets with only **0.14%**, **0.02%**, **1.4%** and **0.65%** labeled pixels in terms of DSC. Representative visualization results are shown in Fig. 8.

2) *Comparison with NLL methods*: In Table IV, we also compare YoloCurvSeg with several NLL methods, including generalized cross-entropy loss (GCE), co-teaching (COT), TriNet, confident learning with spatial label smoothing (CLS LS) and divergence-aware selective training (DAST) on OCTA500 and DRIVE. Despite utilizing one full mask and multiple or even all skeleton samples, these methods are inferior to YoloCurvSeg which employs only one skeleton sample. We also find that all NLL methods perform worse than the fully-supervised model (FS in Table IV) trained solely with the same single fully labeled sample, illustrating that

TABLE III

COMPARISON WITH EXISTING WSL METHODS ON THE FOUR DATASETS. THE BEST RESULTS ARE HIGHLIGHTED IN BOLD AND RED, AND THE SECOND-BEST RESULTS ARE HIGHLIGHTED IN BLUE. **FS** DENOTES FULLY-SUPERVISED LEARNING.

Sample Size	Method	OCTA500		CORN		DRIVE		CHASEDB1	
		DSC \uparrow	ASSD \downarrow	DSC \uparrow	ASSD \downarrow	DSC \uparrow	ASSD \downarrow	DSC \uparrow	ASSD \downarrow
All	pCE [20]	67.23 \pm 4.71	2.50 \pm 0.83	42.47 \pm 5.66	8.01 \pm 4.90	62.59 \pm 5.82	4.60 \pm 0.87	55.20 \pm 3.13	10.09 \pm 2.02
	RW [77]	61.54 \pm 4.19	2.91 \pm 0.92	32.44 \pm 6.07	8.40 \pm 4.46	42.13 \pm 3.05	9.86 \pm 1.50	39.34 \pm 3.11	14.23 \pm 1.44
	USTM [78]	71.59 \pm 3.23	1.78\pm0.51	40.70 \pm 5.49	8.93 \pm 5.74	62.52 \pm 6.26	4.71 \pm 0.81	56.74 \pm 2.48	7.43 \pm 1.18
	S2L [79]	69.54 \pm 5.11	2.43 \pm 0.83	41.47 \pm 7.22	8.81 \pm 4.22	56.81 \pm 3.45	5.71 \pm 0.98	61.75 \pm 3.29	7.28 \pm 1.11
	MLoss [80]	72.16\pm3.73	2.03 \pm 0.72	45.34 \pm 3.59	6.53 \pm 3.39	58.62 \pm 4.88	4.65 \pm 0.58	63.82 \pm 2.85	5.74 \pm 1.42
	EM [81]	71.08 \pm 3.54	1.92 \pm 0.64	41.92 \pm 3.02	7.18 \pm 2.76	61.64 \pm 3.99	5.19 \pm 1.05	54.37 \pm 2.94	9.23 \pm 2.26
	Dense CRF [21]	71.84 \pm 3.52	2.05 \pm 0.66	45.56 \pm 7.24	8.55 \pm 5.55	58.88 \pm 4.29	4.23 \pm 0.57	56.48 \pm 5.28	9.23 \pm 2.12
	Gated CRF [82]	70.18 \pm 4.10	2.80 \pm 0.86	45.24 \pm 7.32	7.64 \pm 4.52	47.81 \pm 3.69	8.46 \pm 1.31	51.54 \pm 3.16	9.69 \pm 1.42
	AC [83]	70.10 \pm 3.04	1.93 \pm 0.43	41.49 \pm 8.46	7.91 \pm 4.39	62.41 \pm 6.40	5.39 \pm 1.36	54.89 \pm 2.00	9.48 \pm 3.08
	DBDM [23]	71.37 \pm 3.88	2.01 \pm 0.73	43.78 \pm 9.30	7.66 \pm 4.07	64.18\pm3.88	3.36\pm0.66	53.87 \pm 4.24	10.25 \pm 3.25
	Tree Energy [18]	72.09 \pm 4.06	2.18 \pm 0.77	51.22\pm4.33	5.29\pm2.31	60.21 \pm 4.39	6.50 \pm 1.70	73.07\pm1.75	3.71\pm0.95
	Ours (coarse)	85.10\pm2.78	0.90\pm0.33	72.15\pm5.61	3.53\pm2.20	78.30\pm2.04	1.59\pm0.30	78.32\pm2.63	3.22\pm0.78
	FS	88.76 \pm 2.86	0.63 \pm 0.33	67.19 \pm 6.67	3.83 \pm 2.17	81.84 \pm 1.47	1.19 \pm 0.20	81.29 \pm 1.59	2.45 \pm 0.47
One	pCE [20]	67.99 \pm 4.76	3.13 \pm 0.91	37.74 \pm 10.80	12.14 \pm 6.24	55.84 \pm 5.85	4.59\pm0.59	52.62 \pm 1.92	9.07 \pm 2.10
	RW [77]	62.02 \pm 4.24	3.75 \pm 1.01	23.54 \pm 7.71	17.10 \pm 9.33	39.43 \pm 3.30	13.62 \pm 2.78	40.41 \pm 1.71	13.38 \pm 1.31
	USTM [78]	67.00 \pm 4.04	3.13 \pm 0.85	42.55 \pm 7.80	8.86 \pm 5.70	56.07 \pm 4.03	6.57 \pm 1.20	50.73 \pm 6.40	15.65 \pm 5.77
	S2L [79]	66.60 \pm 4.02	2.72 \pm 0.74	39.65 \pm 9.09	9.71 \pm 4.74	54.96 \pm 4.41	5.74 \pm 1.10	54.66 \pm 2.44	10.56 \pm 4.63
	MLoss [80]	67.06 \pm 3.94	2.96 \pm 0.83	39.45 \pm 7.79	10.35 \pm 5.52	55.94\pm5.05	5.78 \pm 1.14	53.05 \pm 1.10	9.46 \pm 2.82
	EM [81]	67.52 \pm 4.67	2.91 \pm 0.84	38.40 \pm 9.58	10.95 \pm 5.71	47.89 \pm 6.25	7.06 \pm 1.95	52.26 \pm 2.53	9.48 \pm 1.95
	Dense CRF [21]	68.56 \pm 4.52	2.94 \pm 0.87	35.49 \pm 8.72	10.99 \pm 5.67	53.14 \pm 5.33	5.67 \pm 1.08	52.15 \pm 1.17	12.91 \pm 5.86
	Gated CRF [82]	69.01\pm4.17	2.54\pm0.79	38.23 \pm 11.23	11.42 \pm 5.93	40.80 \pm 3.37	9.78 \pm 1.18	47.54 \pm 2.95	11.30 \pm 2.35
	AC [83]	65.80 \pm 5.09	3.89 \pm 1.08	37.51 \pm 9.15	11.21 \pm 6.03	53.73 \pm 7.89	6.31 \pm 1.70	52.54 \pm 2.03	10.91 \pm 4.41
	DBDM [23]	66.22 \pm 4.26	2.86 \pm 0.78	41.09 \pm 7.30	8.26 \pm 4.71	52.99 \pm 4.31	7.03 \pm 1.37	53.29 \pm 2.39	11.42 \pm 2.31
	Tree Energy [18]	64.89 \pm 4.17	3.36 \pm 0.89	53.52\pm9.03	7.18\pm5.07	51.09 \pm 4.49	6.19 \pm 1.13	67.20\pm2.13	5.69\pm1.80
	Ours (coarse)	85.38\pm2.57	0.83\pm0.28	71.45\pm6.48	4.01\pm2.59	77.99\pm1.97	1.71\pm0.34	78.20\pm2.50	2.86\pm0.68
	FS	84.37 \pm 3.77	1.02 \pm 0.47	43.23 \pm 9.01	10.09 \pm 4.40	76.89 \pm 2.52	2.05 \pm 0.49	66.00 \pm 8.11	6.51 \pm 2.35

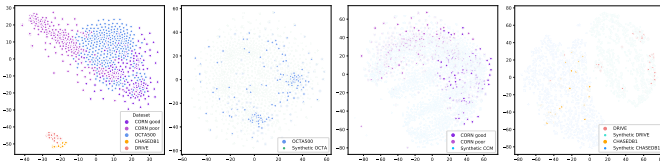


FIG. 6. t-SNE visualization of the four real and synthetic datasets. **CORN good** and **CORN poor** respectively denote the high-quality and low-quality subsets in CORN.

additional noisily labeled samples are not beneficial to model performance under such noisy conditions.

E. Robustness Analysis and Ablation Study

To verify the robustness of YoloCurvSeg for the selected one-shot sparsely labeled sample, we randomly select 10 samples from each dataset and compare the performance with the fully-supervised model trained on the same sample. As demonstrated in Fig. 7, YoloCurvSeg exceeds full supervision in almost all cases and delivers highly stable performance decoupled from image/annotation quality which nevertheless induces great fluctuations in the performance of the fully-supervised models. In addition to robustness, the predictions from YoloCurvSeg also have smaller variances. Both aspects indicate that YoloCurvSeg is sample-insensitive and can reduce the risk of selecting a wrong sample to label.

As for the ablation study, we first remove the background bank extracted by the *Inpainter* and perform direct curve-to-image translation. As shown in panel (a) of Fig. 9, the synthetic

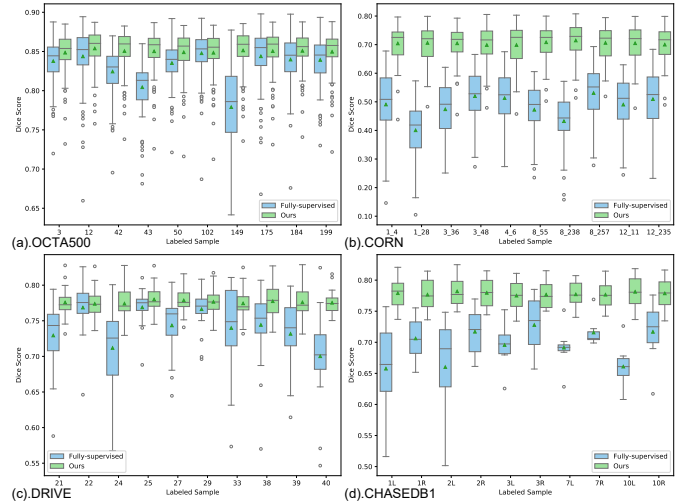


Fig. 7. Performance of YoloCurvSeg given different labeled samples.

images present unrealistic background texture due to the large gap between pre- and post-translation distributions (which is also shown in column B of Table II). For high-resolution image datasets, the foregrounds of the synthetic images are distorted and fail to spatially align with the corresponding curve masks, which also occurs when we remove \mathcal{L}_c of the *Synthesizer* (and use CycleGAN [67] for substitution), as shown in Fig. 9 (b). This indicates that the contrastive *Synthesizer* (especially \mathcal{L}_c) is crucial for maintaining the corresponding local context at the same spatial location.

It is worth pointing out that the results we have reported in the previous section represent the performance of S_{coarse} . We also explore the performance of S_{fine} with and without utilizing \mathcal{D}_{syn} . It can be observed in Fig. 10 that the performance of S_{fine} is further improved by utilizing \mathcal{D}_{syn} , which may be attributed to the fact that the synthetic curves have high degrees of continuity and can reduce the model's outlier predictions. We also conduct a performance comparison of the fully-supervised model with and without pretraining on \mathcal{D}_{syn} . Results show that the synthetic images from YoloCurvSeg also have great potential in serving as pretraining images; pretrain-

TABLE IV

COMPARISON WITH NLL METHODS ON OCTA500 AND DRIVE. **M** AND **S** RESPECTIVELY INDICATE FULL MASK AND NOISY SKELETON. **FS** DENOTES FULLY-SUPERVISED LEARNING.

Method	Label	OCTA500		Label	DRIVE	
		DSC \uparrow	ASSD \downarrow		DSC \uparrow	ASSD \downarrow
GCE [84]	200S	80.34	0.94	20S	73.79	1.83
GCE [84]	1M&199S	80.57	0.90	1M&19S	74.42	2.10
COT [85]	200S	76.59	1.38	20S	73.32	2.40
COT [85]	1M&199S	77.49	1.36	1M&19S	73.82	2.43
TriNet [86]	200S	77.90	1.23	20S	75.47	1.88
TriNet [86]	1M&199S	78.10	1.20	1M&19S	75.53	1.90
CLSLS [87]	200S	80.56	0.96	20S	73.72	1.86
CLSLS [87]	1M&199S	80.59	0.89	1M&19S	74.25	2.07
DAST [88]	1M&199S	65.99	3.02	1M&19S	76.33	2.08
Ours (coarse)	1S	85.38	0.83	1S	77.99	1.71
FS	1M	84.37	1.02	1M	76.89	2.05

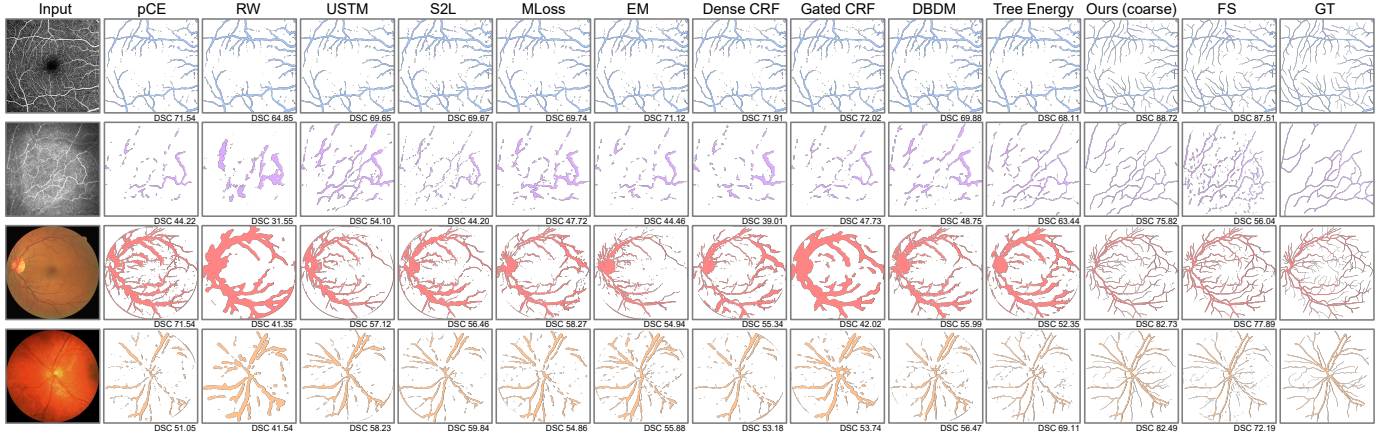


Fig. 8. Qualitative visualization of representative results from our S_{coarse} and other SOTA WSL methods under one-shot setting.

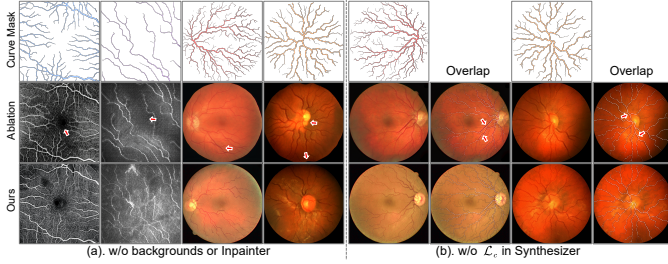


Fig. 9. Visualization of representative synthetic results from the ablation study. Arrows mark the unrealistic background regions, structures, or misalignments between the masks and the regions of interest.

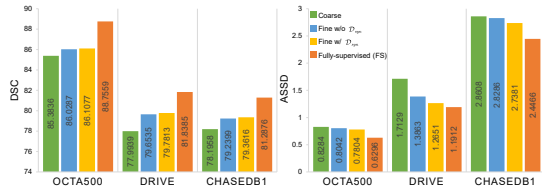


Fig. 10. Performance of YoloCurvSeg under different training paradigms. FS denotes fully-supervised learning.

ing on D_{syn} increases DSC by 0.57, 0.63, 0.81 and decreases ASSD by 0.061, 0.041, 0.148, respectively on OCTA500, DRIVE and CHASEDB1. Ultimately, via further utilizing an additional unlabeled dataset D_{ori} , YoloCurvSeg achieves **97.01%**, **97.49%** and **97.63%** of the fully-supervised performance (with the full masks of all samples employed) with only one noisy skeleton annotation on those three datasets.

V. CONCLUSION

This paper presents a novel sparsely annotated segmentation framework for curvilinear structures, named YoloCurvSeg. Extensive experiments are conducted on four publicly accessible datasets, with superiority of our proposed framework being successfully established. Potential future directions are transferring YoloCurvSeg to 3D scenarios and exploring a better pipeline to further reduce the domain gap between synthetic images and real images.

REFERENCES

- [1] N. Pritchard et al., "Longitudinal assessment of neuropathy in type 1 diabetes using novel ophthalmic markers (LANDMark): study design and baseline characteristics," *Diabetes research and clinical practice*, vol. 104, no. 2, pp. 248–256, May. 2014.
- [2] L. Lin et al., "Blu-gan: Bi-directional convlstm u-net with generative adversarial training for retinal vessel segmentation," in *BenchCouncil International Federated Intelligent Computing and Block Chain Conferences*. Springer, 2020, pp. 3–13.
- [3] R. Kawasaki et al., "Retinal vessel diameters and risk of hypertension: the Multiethnic Study of Atherosclerosis," *Journal of hypertension*, vol. 27, no. 12, pp. 2386–2393, Dec. 2009.
- [4] L. Lin et al., "The SUSTech-SYSU dataset for automated exudate detection and diabetic retinopathy grading," *Scientific data*, vol. 7, no. 1, p. 1–10, 2020.
- [5] R. Allon et al., "Retinal microvascular signs as screening and prognostic factors for cardiac disease: a systematic review of current evidence," *The American Journal of Medicine*, vol. 134, no. 1, pp. 36–47, Jan. 2021.
- [6] L. Lin et al., "Bsda-net: A boundary shape and distance aware joint learning framework for segmenting and classifying octa images," in *MICCAI*. Springer, 2021, pp. 65–75.
- [7] U. T.V. Nguyen et al., "An effective retinal blood vessel segmentation method using multi-scale line detection," *Pattern recognition*, vol. 46, no. 3, pp. 703–715, Mar. 2013.
- [8] N. P. Singh et al., "Retinal blood vessels segmentation by using Gumbel probability distribution function based matched filter," *Computer methods and programs in biomedicine*, vol. 129, pp. 40–50, Jun. 2016.
- [9] L. Peng et al., "Fargo: A joint framework for faz and rv segmentation from octa images," in *International Workshop on Ophthalmic Medical Image Analysis*, Springer, 2021, pp. 42–51.
- [10] L. Mou et al., "CS2-Net: Deep learning segmentation of curvilinear structures in medical imaging," *Medical image analysis*, vol. 67, pp. 101874, Jan. 2021.
- [11] Y. He et al., "Curv-Net: Curvilinear structure segmentation network based on selective kernel and multi-Bi-ConvLSTM," *Medical physics*, vol. 49, no. 5, pp. 3144–3158, Feb. 2022.
- [12] J. Son et al., "Towards accurate segmentation of retinal vessels and the optic disc in fundoscopic images with generative adversarial networks," *Journal of digital imaging*, vol. 32, no. 3, pp. 499–512, Jun. 2019.
- [13] M. Cheng et al., "Joint Topology-Preserving and Feature-Refinement Network for Curvilinear Structure Segmentation," in *ICCV*. 2021, pp. 7147–7156.
- [14] S. Shit et al., "cIDice - A novel topology-preserving loss function for tubular structure segmentation," in *CVPR*. 2021, pp. 16560–16569.
- [15] X. Xu et al., "SemiCurv: Semi-supervised curvilinear structure segmentation," *IEEE Transactions on Image Processing*, vol. 31, pp. 5109–5120, Jul. 2022.
- [16] J. Hou et al., "Semi-supervised semantic segmentation of vessel images using leaking perturbations," in *WACV*. 2022, pp. 2625–2634.
- [17] S. Mittal et al., "Semi-supervised semantic segmentation with high- and low-level consistency," *IEEE transactions on pattern analysis and machine intelligence*, vol. 43, no. 4, pp. 1369–1379, Dec. 2019.
- [18] Z. Liang et al., "Tree energy loss: Towards sparsely annotated semantic segmentation," in *CVPR*. 2022, pp. 16907–16916.
- [19] D. Lin et al., "ScribbleSup: Scribble-supervised convolutional networks for semantic segmentation," in *CVPR*. 2016, pp. 3159–3167.
- [20] M. Tang et al., "Normalized cut loss for weakly-supervised semantic segmentation," in *CVPR*. 2018, pp. 1818–1827.
- [21] M. Tang et al., "On Regularized losses for weakly-supervised CNN segmentation," in *ECCV*. 2018, pp. 507–522.
- [22] H. Kervadea et al., "Constrained-CNN losses for weakly supervised segmentation," *Medical image analysis*, vol. 54, pp. 88–99, May. 2019.
- [23] X. Luo et al., "Scribble-supervised medical image segmentation via dual-Branch network and dynamically mixed pseudo labels supervision," in *MICCAI*. Springer, 2022, pp. 528–538.
- [24] Z. Ji et al., "Scribble-based hierarchical weakly supervised learning for brain tumor segmentation," in *MICCAI*. Springer, 2019, pp. 175–183.
- [25] X. Huo et al., "ATSO: Asynchronous teacher-student optimization for semi-supervised image segmentation," in *CVPR*. 2021, pp. 1235–1244.

- [26] A. J. Larrazabal et al., "Post-DAE: anatomically plausible segmentation via post-processing with denoising autoencoders," *IEEE transactions on medical imaging*, vol. 39, no. 12, pp. 3813–3820, Dec. 2020.
- [27] G. Valvano et al., "Learning to segment from scribbles using multi-scale adversarial attention gates," *IEEE transactions on medical imaging*, vol. 40, no. 8, pp. 1990–2001, Mar. 2021.
- [28] P. Zhang et al., "ACCL: Adversarial constrained-CNN loss for weakly supervised medical image segmentation," *arXiv preprint arXiv:2005.00328*, 2020.
- [29] M. Li et al., "Image projection network: 3D to 2D image segmentation in OCTA images," *IEEE transactions on medical imaging*, vol. 39, no. 11, pp. 3343–3354, May. 2020.
- [30] Y. Zhao et al., "Automated tortuosity analysis of nerve fibers in corneal confocal microscopy," *IEEE transactions on medical imaging*, vol. 39, no. 9, pp. 2725–2737, Feb. 2020.
- [31] J. Staal et al., "Ridge-based vessel segmentation in color images of the retina," *IEEE transactions on medical imaging*, vol. 23, no. 4, pp. 501–509, Apr. 2004.
- [32] M. M. Fraz et al., "An ensemble classification-based approach applied to retinal blood vessel segmentation," *IEEE transactions on biomedical engineering*, vol. 59, no. 9, pp. 2538–2548, Jun. 2012.
- [33] F. Zana et al., "Segmentation of vessel-like patterns using mathematical morphology and curvature evaluation," *IEEE transactions on medical imaging*, vol. 10, no. 7, pp. 1010–1019, Jul. 2001.
- [34] N. Passat et al., "Magnetic resonance angiography: From anatomical knowledge modeling to vessel segmentation," *Medical image analysis*, vol. 10, no. 2, pp. 259–274, Apr. 2006.
- [35] A. F. Frangi et al., "Multiscale vessel enhancement filtering," in *MICCAI*. Springer, 1998, pp. 130–137.
- [36] A. D. Hoover et al., "Locating blood vessels in retinal images by piecewise threshold probing of a matched filter response," *IEEE transactions on medical imaging*, vol. 19, no. 3, pp. 203–210, Mar. 2000.
- [37] J.V.B. Soares et al., "Retinal vessel segmentation using the 2-D Gabor wavelet and supervised classification," *IEEE transactions on medical imaging*, vol. 25, no. 9, pp. 1214–1222, Aug. 2006.
- [38] Y. Zhao et al., "Automatic 2-D/3-D vessel enhancement in multiple modality images using a weighted symmetry filter," *IEEE transactions on medical imaging*, vol. 37, no. 2, pp. 438–450, Sep. 2017.
- [39] J. Zhang et al., "Retinal vessel delineation using a brain-inspired wavelet transform and random forest," *Pattern Recognition*, vol. 69, pp. 107–123, Sep. 2017.
- [40] C. Holbura et al., "Retinal vessels segmentation using supervised classifiers decisions fusion," in *AQTR*. 2012, pp. 185–190.
- [41] O. Ronneberger et al., "U-net: Convolutional networks for biomedical image segmentation," in *MICCAI*. Springer, 2015, pp. 234–241.
- [42] Y. Wu et al., "Multiscale network followed network model for retinal vessel segmentation," in *MICCAI*. Springer, 2018, pp. 19–126.
- [43] J. Hao et al., "Retinal structure detection in OCTA image via voting-based multi-task learning," *IEEE transactions on medical imaging*, early access, Aug. 2022.
- [44] H. Yu et al., "Vision transformer-based retina vessel segmentation with deep adaptive gamma correction," in *ICASSP*. 2022, pp. 1456–1460.
- [45] I. Goodfellow et al., "Generative adversarial networks," *Communications of the ACM*, vol. 63, no. 11, pp. 139–144, Jan. 2020.
- [46] Y. Zhou et al., "DR-GAN: Conditional generative adversarial network for fine-grained lesion synthesis on diabetic retinopathy images," *IEEE journal of biomedical and health informatics*, vol. 26, no. 1, pp. 56–66, Dec. 2020.
- [47] L. Peng et al., "Unsupervised domain adaptation for cross-modality retinal vessel segmentation via disentangling representation style transfer and collaborative consistency learning," in *ISBI*. 2022, pp. 1–5.
- [48] P. Cheng et al., "I-secret: Importance-guided fundus image enhancement via semi-supervised contrastive constraining," in *MICCAI*. Springer, 2021, pp. 87–96.
- [49] Z. Huang et al., "DS3-Net: Difficulty-perceived common-to-t1ce semi-supervised multimodal MRI synthesis network," in *MICCAI*. Springer, 2022, pp. 571–581.
- [50] P. Costa et al., "Towards adversarial retinal image synthesis," *arXiv preprint arXiv:1701.08974*, 2017.
- [51] P. Costa et al., "End-to-end adversarial retinal image synthesis," *IEEE transactions on medical imaging*, vol. 37, no. 3, pp. 781–791, Oct. 2017.
- [52] P. Isola et al., "Image-to-image translation with conditional adversarial networks," in *CVPR*. 2017, pp. 1125–1134.
- [53] J. T. Guibas et al., "Synthetic medical images from dual generative adversarial networks," *arXiv preprint arXiv:1709.01872*. 2017.
- [54] H. Zhao et al., "Synthesizing retinal and neuronal images with generative adversarial nets," *Medical image analysis*, vol. 49, pp. 14–26, Oct. 2018.
- [55] T. Zhang et al., "SkrGAN: Sketching-rendering unconditional generative adversarial networks for medical image synthesis," in *MICCAI*. Springer, 2019, pp. 777–785.
- [56] L. Lin et al., "Automated segmentation of corneal nerves in confocal microscopy via contrastive learning based synthesis and quality enhancement," in *ISBI*. 2021, pp. 1314–1318.
- [57] A. Runions et al., "Modeling trees with a space colonization algorithm," in *Eurographics Workshop on Natural Phenomena*. 2007, pp. 63–70.
- [58] A. Runions et al., "Modeling and visualization of leaf venation patterns," in *ACM SIGGRAPH*. 2005, pp. 702–711.
- [59] P. R. Painter et al., "Pulsatile blood flow, shear force, energy dissipation and Murray's Law," *Theoretical biology and medical modeling*, vol. 3, no. 1, pp. 1–10, Aug. 2006.
- [60] R. Suvorov et al., "Resolution-robust large mask inpainting with fourier convolutions," in *WACV*. 2022, pp. 2149–2159.
- [61] L. Chi et al., "Fast fourier convolution," in *NeurIPS*. 2020, pp. 4479–4488.
- [62] K. He et al., "Deep residual learning for image recognition," in *CVPR*. 2016, pp. 770–778.
- [63] J. Johnson et al., "Perceptual losses for real-time style transfer and super-resolution," in *ECCV*. Springer, 2016, pp. 694–711.
- [64] A. Ross et al., "Improving the adversarial robustness and interpretability of deep neural networks by regularizing their input gradients," in *AAAI*. 2018, vol. 32, no. 1.
- [65] T.-C. Wang et al., "High-resolution image synthesis and semantic manipulation with conditional gans," in *CVPR*. 2018, pp. 8798–8807.
- [66] B. Zhou et al., "Places: A 10 million image database for scene recognition," *IEEE transactions on pattern analysis and machine intelligence*, vol. 40, no. 6, pp. 1452–1464, Jul. 2017.
- [67] J. Zhu et al., "Unpaired image-to-image translation using cycle-consistent adversarial networks," in *ICCV*. 2017, pp. 2223–2232.
- [68] T. Chen et al., "A simple framework for contrastive learning of visual representations," in *ICLR*. 2020, pp. 1597–1607.
- [69] T. Park et al., "Contrastive learning for unpaired image-to-image translation," in *ECCV*. Springer, 2020, pp. 319–345.
- [70] A. Oord et al., "Representation learning with contrastive predictive coding," *arXiv preprint arXiv:1807.03748*, 2018.
- [71] X. Mao et al., "Least squares generative adversarial networks," in *CVPR*. 2017, pp. 2794–2802.
- [72] Z. Zhou et al., "Models genesis: Generic autodidactic models for 3d medical image analysis," in *MICCAI*. Springer, 2019, pp. 384–393.
- [73] P. Mishra et al., "Polynomial learning rate policy with warm restart for deep neural network," in *TENCON*. 2019, pp. 2087–2092.
- [74] S. van der Walt et al., "Scikit-image: Image processing in python," *PeerJ*, vol. 2, p. e453, 2014.
- [75] L. van der Maaten et al., "Visualizing data using t-SNE," *Journal of machine learning research*, vol. 9, no. 11, pp. 2579–2605, Nov. 2008.
- [76] M. Heusel et al., "Gans trained by a two time-scale update rule converge to a local nash equilibrium," in *NeurIPS*. 2017, pp. 6626–6637.
- [77] L. Grady, "Random walks for image segmentation," *IEEE transactions on pattern analysis and machine intelligence*, vol. 28, no. 11, pp. 1768–1783, Nov. 2006.
- [78] X. Liu et al., "Weakly supervised segmentation of COVID19 infection with scribble annotation on CT images," *Pattern recognition*, vol. 122, p. 108341, Feb. 2022.
- [79] H. Lee et al., "Scribble2label: Scribble-supervised cell segmentation via self-generating pseudo-labels with consistency," in *MICCAI*. Springer, 2020, pp. 14–23.
- [80] B. Kim et al., "Mumford-Shah loss functional for image segmentation with deep learning," *IEEE transactions on image processing*, vol. 29, pp. 1856–1866, Sep. 2019.
- [81] Y. Grandvalet et al., "Semi-supervised learning by entropy minimization," in *NeurIPS*. 2004, pp. 281–296.
- [82] A. Obukhov et al., "Gated CRF loss for weakly supervised semantic image segmentation," *arXiv preprint arXiv:1906.04651*, 2019.
- [83] X. Chen et al., "Learning active contour models for medical image segmentation," in *CVPR*. 2019, pp. 11632–11640.
- [84] Z. Zhang et al., "Generalized cross entropy loss for training deep neural networks with noisy labels," in *NeurIPS*. 2018, pp. 1–10.
- [85] B. Han et al., "Co-teaching: Robust training of deep neural networks with extremely noisy labels," in *NeurIPS*. 2018, pp. 1020–1030.
- [86] T. Zhang et al., "Robust medical image segmentation from non-expert annotations with tri-network," in *MICCAI*. Springer, 2020, pp. 249–258.
- [87] M. Zhang et al., "Characterizing label errors: confident learning for noisy-labeled image segmentation," in *MICCAI*. Springer, 2020, pp. 721–730.
- [88] S. Yang et al., "Learning COVID-19 pneumonia lesion segmentation from imperfect annotations via divergence-aware selective training," *JBHI*, vol. 26, pp. 3673–3684, May. 2022.